pp 1943–1966. © Royal Aeronautical Society 2018
doi: 10.1017/aer.2018.104

Low-velocity impact response of sandwich cylindrical panels with nanotube-reinforced and metal face sheet in thermal environment

M. R. Bayat and M. Mosavi Mashhadi
mrb.bayat@gmail.com
Department of Mechanical Engineering
College of Engineering
University of Tehran
Tehran, Iran

O. Rahmani
Smart Structures and New Advanced Materials Laboratory
Department of Mechanical Engineering
University of Zanjan
Zanjan, Iran

ABSTRACT

Employing an analytical method, non-linear low-velocity impact response of carbon nanotube (CNT)-reinforced sandwich cylindrical panels in thermal environments is analysed. Two types of core (i.e. homogenous and functionally graded) are considered for sandwich panels. The face sheets of sandwich panels are multi-layer which consist of CNT-reinforced composite (CNTRC) and metal layers. Micromechanical models are used to estimate the material properties of CNTRCs. A higher-order shear deformation theory with a von Kármán-type of kinematic non-linearity provides the equations of motion. Temperature-dependent material properties are used to include the thermal effects. The equations of motion are solved using a two-step perturbation technique. Existing numerical results in the literature are used to validate the present method. The effect of nanotube volume fraction, material property gradient, impactor initial velocity, geometrical parameters of cylindrical panel, temperature change and edge boundary condition on the impact response of cylindrical panel structures is discussed. The quantitative results and analytical formulations can be helpful in better designing of CNTRC structures subjected to low-velocity impact in thermal environments.

Keywords: Carbon nanotube-reinforced composite; low-velocity impact; thermal loading; analytical modelling; two-step perturbation

Received 17 August 2017; revised 27 April 2018; accepted 1 August 2018.

NOMENCLATURE

a	length in the X direction
b	length in the Y direction
E^{i}	Young's modulus of impactor
E^{m}	Young's modulus of matrix
E_0	reference value of Young's modulus of panel
E_{11}	longitudinal effective Young's modulus
E_{11}^{CN}	longitudinal carbon nanotube Young's modulus
E_{22}	transverse effective Young's modulus
E_{22}^{CN}	transverse carbon nanotube Young's modulus
E_{22}^{s}	transverse Young's moduli of the surface the panel
$\overline{F}(X, Y)$	stress function
G^{m}	shear moduli of matrix
G_{12}	shear moduli of the orthotropic layer
G_{12}^{CN}	in-plane shear modulus of carbon nanotube
h	total thickness of panel
h_{c}	thickness of core
h_{f}	thickness of face sheet
K_{c}	contact stiffness
m^{i}	mass of impactor
$\overline{M}^T$	moment
$\overline{M}_x$, $\overline{M}_y$	bending moments
$\overline{N}^T$	force
$\overline{N}_x$, $\overline{N}_y$, $\overline{N}_{xy}$	stress resultants
P_{c}	the overall contact force
$P_{\max}$	maximum contact force
$\overline{P}^T$	higher order moment
$\overline{P}_x$, $\overline{P}_y$	higher order moments
$\overline{Q}_{ij}$	transformed elastic constants
R	curvature radius of panel
R^c	radius of the panel
R^i	radius of impactor
T_0	reference temperature
$\overline{U}$	panel displacement in the direction of X
V_0	initial velocity of impactor
$\overline{V}$	panel displacement in the direction of Y
V_{CN}	volume fraction of carbon nanotube
V_{m}	volume fraction of matrix
$\overline{W}$	panel displacement in the direction of Z
X, Y, and Z	directions of co-ordinate system

Greek symbol

α^{m}	thermal expansion of matrix
α_{11}	effective longitudinal thermal expansion coefficient
$\alpha_{11}^{\mathrm{CN}}$	longitudinal thermal expansion coefficient of carbon nanotube
α_{22}	effective transverse thermal expansion coefficient

https://doi.org/10.1017/aer.2018.104 Published online by Cambridge University Press

α_{22}^{CN}	transverse thermal expansion coefficient of carbon nanotube
$\delta(t)$	local contact indentation
δ_{max}	maximum local indentation
ΔT	temperature change
η_i	efficiency parameters of carbon nanotube
ν_i	Poisson's ratios of impactor
ν_{12}, ν_{21}	Poisson's ratios of the orthotropic layer
ρ^{CN}	density of carbon nanotube
ρ^{m}	density of matrix
ρ_0	reference value of panel density
$\overline{\Psi}_x$	the mid-plane rotation of normal about the Y axis
$\overline{\Psi}_y$	the mid-plane rotation of normal about the X-axis

1.0 INTRODUCTION

Due to their outstanding mechanical, thermal and electrical properties[1–3], carbon nanotubes (CNTs) are regarded as one the most favourable reinforcement materials for high-strength and light-weighted polymer composites. Dissimilar to carbon fibre-reinforced composites, only a low percentage of CNTs (2–5 wt%)[4,5] are allowed in CNT-reinforced composites (CNTRCs) because more volume fraction beyond a certain limit will worsen their mechanical properties[6]. Hence, the idea of functionally graded (FG) materials was employed in order to optimally utilise the CNT reinforcement effect. Shen[7] first applied the concept of FG materials to nanocomposites and investigated the non-linear bending behaviour of CNTRC plates and observed that the plate load-bending moment curves significantly improved due to the FG distribution of CNTs through the thickness. Also, Kwon et al.[8] proposed a powder metallurgy route for fabricating FG CNT-reinforced aluminium (Al) matrix composite which completely supports the concept of FG nanocomposites. Furthermore, Shen and Xiang[9] investigated non-linear temperature-dependent large amplitude vibration behaviour of FG-CNTRC cylindrical panels resting on elastic foundations. They found that non-linear to linear frequency ratios of CNTRC panels with intermediate volume fraction of CNTs is not necessarily intermediate.

A thick but lightweight material as core, embedded in two thin but stiff materials such as face sheets, forms a structure with high bending stiffness and low overall density, which is called the sandwich structure. Sandwich panels are extensively used in aeronautical and automotive applications as well as civil infrastructure, such as highway bridges[10]. Especially, under impact loading, sandwich panels are susceptible to face sheet/core debonding due to the difference in stiffness properties between core and face sheets[11]. The purpose of this work is to examine the behaviour of CNTRC sandwich panels subjected to low-velocity impact. FG materials usually consist of ceramic and metal phases with varying mechanical properties through the thickness. For further information on FG materials one can refer to Ref. 12. Utilising an FG core in sandwich panels expressively can reduce the face sheet–core interfacial shear stresses and so the possibility of face sheet/core debonding[13].

Fibre–metal laminate (FML) is an advanced hybrid composite material consisting of some thin metal layers bonded with composite material layers. FMLs allow metal benefits such as ductility, damage and impact tolerances to be combined with good features of composite materials such as high specific stiffness and strength, good fatigue and corrosion resistance[14–17]. The combination of metal and composite characteristics in one material makes

https://doi.org/10.1017/aer.2018.104 Published online by Cambridge University Press

FMLs a powerful applicant material for new generation and high-capacity aircraft fuselage skin structures. FMLs also can be used as face sheets in sandwich panels. Tan and Akil[18] explored the impact response of sandwich composite structure with polypropylene honeycomb core and FML face sheet. They found that with increasing impact energy, the maximum impact load increases up to a threshold value and then plateaus while the energy absorption will increase continuously. Similar to FML, CNTRCs can be used to form a CNT–metal laminate (CNTML) composite which consist of thin metal layers such as Al, bonded with CNTRC layers.

Low-velocity impact is one of the most crucial loadings that composite structures experience during their service life, especially for aerospace composite structures[19,20]. Wang et al.[21] studied the low-velocity impact response of foam-core sandwich panels using experimental and numerical approaches. They also explored the effects of impact variables and sandwich panel configuration parameters on the impact behaviour. Jam and Kiani[22] used Timoshenko beam theory to analyse the influences of thermal environment, CNT volume fraction, distribution of CNTs, initial velocity and mass of impactor on low-velocity impact response of FG-CNTRC composite beams. Wang et al.[23] analysed the temperature-dependent low-velocity impact response of single-layer FG-CNTRC as well as sandwich composite plates and examined the effect of various impact and environmental parameters. The low-velocity impact response of Al foam sandwich structures with fibre-reinforced thermoplastic and FML face sheets was modelled using a simple energy-balance model by Kiratisaevee and Cantwell[24]. Using experimental and numerical methods, Meo et al.[25] studied the low-velocity impact response of the composite sandwich panels at five various energy levels. They found that at relatively low impact-energy levels, notable internal damage may occur which could reduce the residual strength of panel significantly.

To the best of the readers' knowledge, and as the literature survey accepts, there is no study neither on the low-velocity impact response of sandwich nor CNTML and FG-CNTRC cylindrical panels. In this study, the non-linear temperature-dependent low-velocity impact response of nanotube-reinforced composite cylindrical panel-type structures is studied. Three types of cylindrical panel configurations (i.e. single-layer, CNTML and sandwich cylindrical panels) are considered in which CNTs are either uniformly distributed (UD) or FG through the thickness direction. In the sandwich configuration, two types of core (i.e. homogenous and FG) are considered embedded in two CNTML face sheets. Micromechanical models are used to estimate the material properties. A higher-order shear deformation theory[26] with a von Kármán-type of kinematic non-linearity[27] and thermal effects is used to form the equations of motion. Material properties of all types of configurations are assumed to be temperature dependent. Two types of boundary conditions (i.e. movable and immovable) are used for all edges of cylindrical panel. The numerical results illustrate the non-linear low-velocity impact response of different kinds of composite cylindrical panels under various sets of environmental conditions.

2.0 NON-LINEAR DYNAMICS OF CNTRC CYLINDRICAL PANELS

The cylindrical panel studied in this paper is composed of two CNTML face sheets and a homogenous or FG core. As shown in Fig. 1, the radius of curvature, total thickness of panel, length in the X and Y directions are designated as R, h, a and b, respectively. The thickness of each face sheets and core is h_f and h_c, respectively. The nanotube reinforcement used in

https://doi.org/10.1017/aer.2018.104 Published online by Cambridge University Press

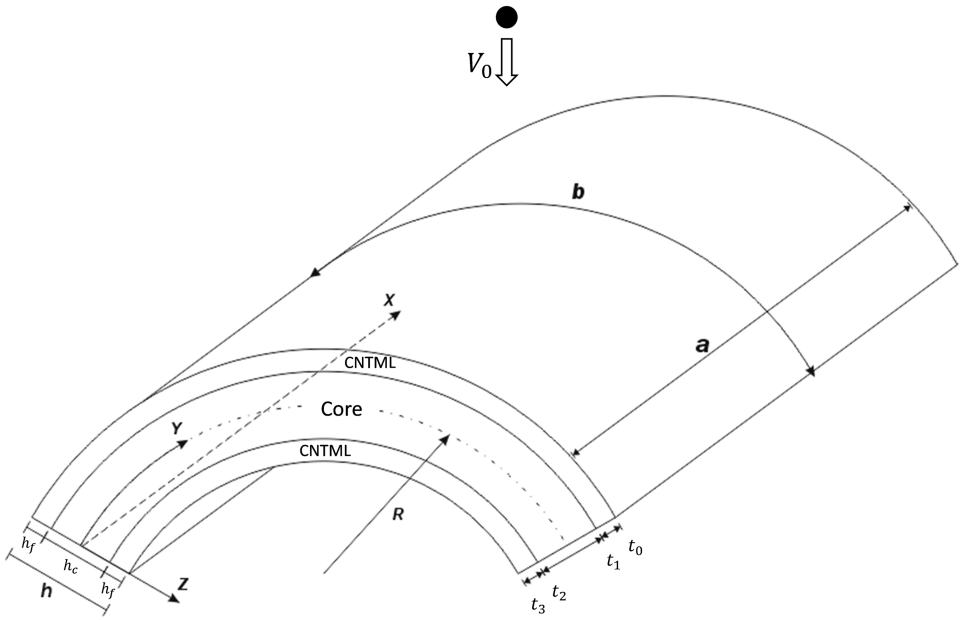

Figure 1. Co-ordinate system and geometry of cylindrical panel subjected to low-velocity impact.

CNTML of face sheets are either UD or FG. The panel is subjected to low-velocity impact in various thermal conditions. The origin of co-ordinate system is at the corner of the panel on the mid-plane (see Fig. 1). Parallel to the right-hand set of axes (X, Y, Z), in which X and Y are in the axial and circumferential directions of the panel and Z is in the direction of the inward normal to the middle surface, panel displacements are designated as $\overline{U}$, $\overline{V}$ and $\overline{W}$. The mid-plane rotations of normal about the Y and X axes are labelled as $\overline{\Psi}_x$ and $\overline{\Psi}_y$, respectively. The stress resultants are given as $\overline{N}_x = \overline{F}_{,YY}$, $\overline{N}_y = \overline{F}_{,XX}$ and $\overline{N}_{xy} = -\overline{F}_{,XY}$, where $\overline{F}(X, Y)$ is the stress function in which partial differential with respect to the corresponding co-ordinates is denoted as comma. It should be noted that all calculations for layers will be carried out using this co-ordinate system.

Reddy and Liu[28] modified Sanders shell theory and developed a higher-order shear deformation shell theory. In this theory, the transverse shear strains are assumed to be parabolically distributed across the shell thickness and the number of independent unknowns ($\overline{U}$, $\overline{V}$, $\overline{W}$, $\overline{\Psi}_x$ and $\overline{\Psi}_y$) is the same as in the first-order shear deformation theory; however, there is no need for the correction factor. The motion equations of cylindrical panel can be expressed in terms of a transverse displacement $\overline{W}$, two rotations $\overline{\Psi}_x$ and $\overline{\Psi}_y$, and a stress function $\overline{F}$, based on Reddy's higher-order shear deformation theory with a von Kármán-type of kinematic non-linearity and thermal effects[9], as follows:

$$\widetilde{L}_{11}(\overline{W}) - \widetilde{L}_{12}(\overline{\Psi}_x) - \widetilde{L}_{13}(\overline{\Psi}_y) + \widetilde{L}_{14}(\overline{F}) - \widetilde{L}_{15}\left(\overline{N}^T\right) - \widetilde{L}_{16}\left(\overline{M}^T\right) - \frac{1}{R}\overline{F}_{,XX}$$
$$= \widetilde{L}(\overline{W}, \overline{F}) + \widetilde{L}_{17}\left(\ddot{\overline{W}}\right) - \left(\widetilde{I}_5 \frac{\partial \ddot{\overline{\Psi}}_x}{\partial X} + \widetilde{I}_5' \frac{\partial \ddot{\overline{\Psi}}_y}{\partial Y}\right) + q \qquad \ldots(1)$$

https://doi.org/10.1017/aer.2018.104 Published online by Cambridge University Press

$$\widetilde{L}_{21}\left(\overline{F}\right)+\widetilde{L}_{22}\left(\overline{\Psi}_x\right)+\widetilde{L}_{23}\left(\overline{\Psi}_y\right)-\widetilde{L}_{24}\left(\overline{W}\right)-\widetilde{L}_{25}\left(\overline{N}^T\right)+\frac{1}{R}\overline{W}_{,XX}=-\frac{1}{2}\widetilde{L}\left(\overline{W},\overline{W}\right) \quad ...(2)$$

$$\widetilde{L}_{31}\left(\overline{W}\right)+\widetilde{L}_{32}\left(\overline{\Psi}_x\right)-\widetilde{L}_{33}\left(\overline{\Psi}_y\right)+\widetilde{L}_{34}\left(\overline{F}\right)-\widetilde{L}_{35}\left(\overline{N}^T\right)-\widetilde{L}_{36}\left(\overline{S}^T\right)=\widehat{I}_5\frac{\partial\ddot{\overline{W}}}{\partial X}-\widehat{I}_3\ddot{\overline{\Psi}}_x \quad ...(3)$$

$$\widetilde{L}_{41}\left(\overline{W}\right)-\widetilde{L}_{42}\left(\overline{\Psi}_x\right)+\widetilde{L}_{43}\left(\overline{\Psi}_y\right)+\widetilde{L}_{44}\left(\overline{F}\right)-\widetilde{L}_{45}\left(\overline{N}^T\right)-\widetilde{L}_{46}\left(\overline{S}^T\right)=\widehat{I}_5'\frac{\partial\ddot{\overline{W}}}{\partial Y}-\widehat{I}_3'\ddot{\overline{\Psi}}_y \quad ...(4)$$

in which

$$\widetilde{L}()=\frac{\partial^2}{\partial X^2}\frac{\partial^2}{\partial Y^2}-2\frac{\partial^2}{\partial X\partial Y}\frac{\partial^2}{\partial Y\partial X}+\frac{\partial^2}{\partial Y^2}\frac{\partial^2}{\partial X^2} \quad ...(5a)$$

$$\widetilde{L}_{17}()=-I_1-\left(\widetilde{I}_7\frac{\partial^2}{\partial X^2}+\widetilde{I}_7'\frac{\partial^2}{\partial Y^2}\right) \quad ...(5b)$$

and the other linear operators $\widetilde{L}_{ij}()$ are given in Refs 29,30. I_j, $\widehat{I}_j$ and $\widetilde{I}_j$ are given in Equation (19) below. The von Kármán type geometric non-linearity is embedded in terms of $\widetilde{L}()$ in Equations (1) and (2). In Equations (1)–(4), differentiation with respect to time is denoted with superposed dots. Forces $\overline{N}^T$, moments $\overline{M}^T$ and higher order moments $\overline{P}^T$ caused by elevated temperature are given by

$$\begin{bmatrix}\overline{N}_x^T & \overline{M}_x^T & \overline{P}_x^T\\ \overline{N}_y^T & \overline{M}_y^T & \overline{P}_y^T\\ \overline{N}_{xy}^T & \overline{M}_{xy}^T & \overline{P}_{xy}^T\end{bmatrix}=\sum_{k=1}\int_{-h/2}^{h/2}\begin{bmatrix}A_x\\A_y\\A_{xy}\end{bmatrix}_k\left(1,Z,Z^3\right)\Delta T\,\mathrm{d}Z \quad ...(6a)$$

$$\begin{bmatrix}\overline{S}_x^T\\ \overline{S}_y^T\\ \overline{S}_{xy}^T\end{bmatrix}=\begin{bmatrix}\overline{M}_x^T\\ \overline{M}_y^T\\ \overline{M}_{xy}^T\end{bmatrix}-\frac{4}{3h^2}\begin{bmatrix}\overline{P}_x^T\\ \overline{P}_y^T\\ \overline{P}_{xy}^T\end{bmatrix} \quad ...(6b)$$

where $\Delta T=T-T_0$ shows the temperature change from reference temperature T_0 in which no thermal strains are available, and

$$\begin{bmatrix}A_x\\A_y\\A_{xy}\end{bmatrix}=-\begin{bmatrix}\overline{Q}_{11} & \overline{Q}_{12} & \overline{Q}_{16}\\ \overline{Q}_{12} & \overline{Q}_{22} & \overline{Q}_{26}\\ \overline{Q}_{16} & \overline{Q}_{26} & \overline{Q}_{66}\end{bmatrix}\begin{bmatrix}1 & 0\\0 & 1\\0 & 0\end{bmatrix}\begin{bmatrix}\alpha_{11}\\ \alpha_{22}\end{bmatrix} \quad ...(7)$$

where longitudinal and transverse thermal expansion coefficients are denoted by α_{11} and α_{22}, respectively; as given in details in Ref. 28, $\overline{Q}_{ij}$ indicate the transformed elastic constants. For an FG-CNTRC layer (i.e. orthotropic layer), $\overline{Q}_{ij}=Q_{ij}$, and

$$Q_{11}=\frac{E_{11}}{1-\nu_{12}\nu_{21}},\quad Q_{22}=\frac{E_{22}}{1-\nu_{12}\nu_{21}},\quad Q_{12}=\frac{\nu_{12}E_{11}}{1-\nu_{12}\nu_{21}}$$
$$Q_{16}=Q_{26}=0,\quad Q_{44}=G_{23},\quad Q_{55}=G_{13},\quad Q_{66}=G_{12} \quad ...(8)$$

in which the longitudinal and transverse effective Young's moduli, shear moduli and Poisson's ratios of the orthotropic layer are designated as E_{11}, E_{22}, G_{12}, ν_{12} and ν_{21}, respectively.

https://doi.org/10.1017/aer.2018.104 Published online by Cambridge University Press

A micromechanical model can be used to predict the effective material properties of CNTRCs[7] as follows:

$$E_{11} = \eta_1 V_{CN} E_{11}^{CN} + V_m E^m \quad ...(9a)$$

$$\frac{\eta_2}{E_{22}} = \frac{V_{CN}}{E_{22}^{CN}} + \frac{V_m}{E^m} \quad ...(9b)$$

$$\frac{\eta_3}{G_{12}} = \frac{V_{CN}}{G_{12}^{CN}} + \frac{V_m}{G^m} \quad ...(9c)$$

where E_{11}^{CN}, E_{22}^{CN} and G_{12}^{CN} are the longitudinal and transverse Young's moduli, and in-plane shear moduli of CNT, respectively and E^m and G^m are the similar properties of the matrix. The CNT efficiency parameters are denoted by η_j ($j = 1, 2, 3$) and are determined later by matching the elastic moduli of CNTRCs obtained from the molecular dynamics (MD) simulations with those of the extended rule of mixture in Equation (9). CNT and the matrix volume fraction are designated as V_{CN} and V_m, respectively, which satisfy the condition of $V_{CN} + V_m = 1$.

The material properties of FG ceramic-metal core studied in this paper change continuously from one side to the other in which the constituent volume fraction can follow a simple power law. While only linear FG-CNTRC materials can be readily achieved in practice[8]. Hence, only the linear distribution of FG-CNTRCs is considered in this study. Three types of FG-CNTRC layers as well as ceramic-metal FG-core are considered in this study: (1) FG-Λ, in which the inner surface of the layer is CNT/ceramic rich; while in (2) FG-V, the outer surface of the layer is CNT/ceramic rich; and finally in (3) FG-X, both outer and inner surfaces are CNT/ceramic rich.

$$\text{For single-layer FG-}\Lambda\text{ CNTRC}: \quad V_{CN} = \left(1 + \frac{2Z}{h}\right) V_{CN}^* \quad ...(10a)$$

$$\text{For single-layer FG-V CNTRC}: \quad V_{CN} = \left(1 + \frac{2Z}{h}\right) V_{CN}^* \quad ...(10b)$$

$$\text{For single-layer FG-X CNTRC}: \quad V_{CN} = 4\frac{|Z|}{h} V_{CN}^* \quad ...(10c)$$

$$\text{For single-layer UD CNTRC}: \quad V_{CN} = V_{CN}^* = \frac{w_{CN}}{w_{CN} + (\rho^{CN}/\rho^m) - (\rho^{CN}/\rho^m) w_{CN}} \quad ...(10d)$$

where the mass fraction of nanotube is designated as w_{CN}, and the densities of matrix and CNT are labelled as ρ^m and ρ^{CN}, respectively. $\rho = V_{CN}\rho^{CN} + V_m\rho^m$ defines the overall mass density of CNTRC. It is notable that both the UD (i.e. $V_{CN} = V_{CN}^*$) and FG CNTRCs will have the same value of CNT mass fractions.

The longitudinal and transverse thermal expansion coefficients are defined as follows:

$$\alpha_{11} = \frac{V_{CN} E_{11}^{CN} \alpha_{11}^{CN} + V_m E^m \alpha^m}{V_{CN} E_{11}^{CN} + V_m E^m} \quad ...(11a)$$

$$\alpha_{22} = \left(1 + \nu_{12}^{CN}\right) V_{CN} \alpha_{22}^{CN} + (1 + \nu^m) V_m \alpha^m - \nu_{12} \alpha_{11} \quad ...(11b)$$

https://doi.org/10.1017/aer.2018.104 Published online by Cambridge University Press

where α^{m} is the matrix thermal expansion coefficient; and α_{11}^{CN} and α_{22}^{CN} indicate the CNT longitudinal and transverse thermal expansion coefficients, which are graded in the thickness direction; also ν^{m} and ν_{12}^{CN} are, respectively, matrix and CNT Poisson's ratios. It should be noted that thermal stress due to different thermal expansion of CNT and matrix is neglected in this study. As in this study, the material properties are assumed to be temperature dependent, the effective material properties of FG-CNTRC vary with position and temperature. However, the effective Poisson's ratio is expressed as

$$\nu_{12} = V_{CN}^{*}\nu_{12}^{CN} + V_{m}\nu^{m} \quad ...(12)$$

because it weakly depends on position and temperature change.

Consequently, the volume fraction of ceramic of the core is as follows:

$$\text{For } \Lambda \text{ type core}: \quad V_c = \left(\frac{1}{2} + \frac{Z}{h_c}\right)^{n} \quad ...(13a)$$

$$\text{For V type core}: \quad V_c = \left(\frac{1}{2} - \frac{Z}{h_c}\right)^{n} \quad ...(13b)$$

$$\text{For X type core}: \quad V_c = \left(2\frac{|Z|}{h_c}\right)^{n} \quad ...(13c)$$

The four edges of the cylindrical panel are supposed to be simply supported with or without in-plane displacement, labelled as 'movable' and 'immovable', as the temperature is increased steadily. Based on the above definition, the boundary conditions are

$$X = 0, a:$$

$$\overline{W} = \overline{\Psi}_y = 0 \quad ...(14a)$$

$$\overline{M}_x = \overline{P}_x = 0 \quad ...(14b)$$

$$\int_0^b \overline{N}_x dY = 0 \text{ (movable)} \quad ...(14c)$$

$$\overline{U} = 0 \text{ (immovable)} \quad ...(14d)$$

$$Y = 0, b:$$

$$\overline{W} = \overline{\Psi}_x = 0 \quad ...(14e)$$

$$\overline{M}_y = \overline{P}_y = 0 \quad ...(14f)$$

$$\int_0^b \overline{N}_y dY = 0 \text{ (movable)} \quad ...(14g)$$

$$\overline{V} = 0 \text{ (immovable)} \quad ...(14h)$$

https://doi.org/10.1017/aer.2018.104 Published online by Cambridge University Press

in which, as defined in Ref. 28, $\overline{M}_x$, $\overline{M}_y$ and $\overline{P}_x$, $\overline{P}_y$ are bending and higher-order moments, respectively. The expressed conditions in Equations (14d) and (14h) are satisfied in the average sense as

$$\int_0^b\int_0^a \frac{\partial \overline{U}}{\partial X}\mathrm{d}X\mathrm{d}Y = 0, \quad \int_0^a\int_0^b \frac{\partial \overline{V}}{\partial Y}\mathrm{d}Y\mathrm{d}X = 0 \qquad ...(15)$$

or

$$\int_0^b\int_0^a \left[A_{11}^*\frac{\partial^2\overline{F}}{\partial Y^2} + A_{12}^*\frac{\partial^2\overline{F}}{\partial X^2} + \left(B_{11}^* - \frac{4}{3h^2}E_{11}^*\right)\frac{\partial\overline{\Psi}_x}{\partial X} + \left(B_{12}^* - \frac{4}{3h^2}E_{12}^*\right)\frac{\partial\overline{\Psi}_y}{\partial Y} - \frac{4}{3h^2}\left(E_{11}^*\frac{\partial^2\overline{W}}{\partial X^2} + E_{12}^*\frac{\partial^2\overline{W}}{\partial Y^2}\right) - \frac{1}{2}\left(\frac{\partial\overline{W}}{\partial X}\right)^2 - \left(A_{11}^*\overline{N}_x^T + A_{12}^*\overline{N}_y^T\right)\right]\mathrm{d}X\mathrm{d}Y = 0 \qquad ...(16a)$$

$$\int_0^a\int_0^b \left[A_{22}^*\frac{\partial^2\overline{F}}{\partial X^2} + A_{12}^*\frac{\partial^2\overline{F}}{\partial Y^2} + \left(B_{21}^* - \frac{4}{3h^2}E_{21}^*\right)\frac{\partial\overline{\Psi}_x}{\partial X} + \left(B_{22}^* - \frac{4}{3h^2}E_{22}^*\right)\frac{\partial\overline{\Psi}_y}{\partial Y} - \frac{4}{3h^2}\left(E_{21}^*\frac{\partial^2\overline{W}}{\partial X^2} + E_{22}^*\frac{\partial^2\overline{W}}{\partial Y^2}\right) + \frac{\overline{W}}{R} - \frac{1}{2}\left(\frac{\partial\overline{W}}{\partial Y}\right)^2 - \left(A_{12}^*\overline{N}_x^T + A_{22}^*\overline{N}_y^T\right)\right]\mathrm{d}Y = 0 \qquad ...(16b)$$

in which the reduced stiffness matrices $\left[A_{ij}^*\right]$, $\left[B_{ij}^*\right]$, $\left[D_{ij}^*\right]$, $\left[E_{ij}^*\right]$, $\left[F_{ij}^*\right]$ and $\left[H_{ij}^*\right]$ that are functions of position and temperature are defined as[27]

$$\mathbf{A}^* = \mathbf{A}^{-1}, \quad \mathbf{B}^* = -\mathbf{A}^{-1}\mathbf{B}, \quad \mathbf{D}^* = \mathbf{D} - \mathbf{B}\mathbf{A}^{-1}\mathbf{B}, \quad \mathbf{E}^* = -\mathbf{A}^{-1}\mathbf{E}, \quad \mathbf{F}^* = \mathbf{F} - \mathbf{E}\mathbf{A}^{-1}\mathbf{B}, \quad \mathbf{H}^* = \mathbf{H} - \mathbf{E}\mathbf{A}^{-1}\mathbf{E} \qquad ...(17)$$

where panel stiffnesses A_{ij}, B_{ij}, etc. are defined as

$$\left(A_{ij}, B_{ij}, D_{ij}, E_{ij}, F_{ij}, H_{ij}\right) = \sum_{k=1}^{t_k}\int_{t_{k-1}} \left(\overline{Q}_{ij}\right)_k \left(1, Z, Z^2, Z^3, Z^4, Z^6\right)\mathrm{d}Z, \quad (i,j = 1,2,6) \qquad ...(18a)$$

$$\left(A_{ij}, D_{ij}, F_{ij}\right) = \sum_{k=1}^{t_k}\int_{t_{k-1}} \left(\overline{Q}_{ij}\right)_k \left(1, Z^2, Z^4\right)\mathrm{d}Z \quad (i,j = 4,5) \qquad ...(18b)$$

The inertias I_i ($i = 1, 2, 3,\ldots,7$) are defined by

$$\left(I_1, I_2, I_3, I_4, I_5, I_7\right) = \sum_{k=1}^{t_k}\int_{t_{k-1}} \rho_k(Z)\left(1, Z, Z^2, Z^3, Z^4, Z^6\right)\mathrm{d}Z \qquad ...(19a)$$

https://doi.org/10.1017/aer.2018.104 Published online by Cambridge University Press

with $c_1 = 4/(3h^2)$, the following variables are defined[9]

$$\bar{I}_1 = I_1, \quad \bar{I}_1' = I_1 + \frac{2}{R} I_2, \quad \bar{I}_2 = I_2 - c_1 I_4, \quad \bar{I}_2' = I_2 + \frac{1}{R} I_3 - c_1 I_4 - \frac{c_1}{R} I_5, \quad \bar{I}_3 = c_1 I_4,$$
$$\bar{I}_3' = c_1 I_4 + \frac{c_1}{R} I_5, \quad \bar{I}_4 = \bar{I}_4' = I_3 - 2c_1 I_5 + c_1^2 I_7, \quad \bar{I}_5 = \bar{I}_5' = c_1 I_5 - c_1^2 I_7,$$
$$\hat{I}_3 = \bar{I}_4 - \frac{\bar{I}_2 \bar{I}_2}{\bar{I}_1}, \quad \hat{I}_3' = \bar{I}_4' - \frac{\bar{I}_2' \bar{I}_2'}{\bar{I}_1'}, \quad \hat{I}_5 = \bar{I}_5 - \frac{\bar{I}_2 \bar{I}_3}{\bar{I}_1}, \quad \hat{I}_5' = \bar{I}_5' - \frac{\bar{I}_2' \bar{I}_3'}{\bar{I}_1'}, \quad \hat{I}_7 = \frac{\bar{I}_3 \bar{I}_3}{\bar{I}_1} - c_1^2 I_7,$$
$$\hat{I}_7' = \frac{\bar{I}_3' \bar{I}_3'}{\bar{I}_1'} - c_1 I_7, \quad \tilde{I}_5 = \hat{I}_3 + \hat{I}_5, \quad \tilde{I}_5' = \hat{I}_3' + \hat{I}_5', \quad \tilde{I}_7 = \hat{I}_7 - \hat{I}_5, \quad \tilde{I}_7' = \hat{I}_7' - \hat{I}_5' \qquad \text{...(19b)}$$

3.0 NON-LINEAR DYNAMICS OF IMPACTOR

In this study, the vibration of impactor is neglected. The overall contact force P_c during the loading phase is related to local contact indentation $\delta(t)$ and defined by a non-linear relation as follows[31,32]:

$$P_c(t) = K_c[\delta(t)]^r \qquad \text{...(20)}$$

According to the Hertzian law for contact between two homogeneous isotropic solids, $r = 1.5$ is considered. In addition, it has been proved that for laminated composite targets, r is also equal to 1.5. The contact stiffness K_c is given by

$$K_c = \frac{4}{3} E^* \sqrt{R^*}, \quad E^* = \left(\frac{1 - \nu^i 2}{E^i} + \frac{1 - \nu_{12}^2}{E_{22}^s} \right), \quad \frac{1}{R^*} = \frac{1}{R^i} + \frac{1}{2R^c} \qquad \text{...(21)}$$

in which E^i, ν^i and R^i are Young's moduli, Poisson's ratio and radius of impactor, respectively; and E_{22}^s and R^c are the transverse Young's moduli of the surface and radius of the panel, respectively.

Through the unloading phase, the contact force is defined as[32]

$$P_c(t) = P_{max} \left[\frac{\delta(t) - \delta_0}{\delta_{max} - \delta_0} \right]^s \qquad \text{...(22)}$$

where P_{max} and δ_{max} are the maximum contact force and the corresponding local indentation through the loading phase, respectively. Through the loading phase, as δ_{max} is blew a critical indentation, there is no permanent indentation δ_0. In Equation (22), s is a curve fitting parameter and is computed by fitting the function in Equation (22) to experimental results. Tests have been indicated that $s = 2.5$ provides a good agreement to experimental results[32].

The local contact indentation is given as

$$\delta(t) = \bar{S}(t) - \bar{W}(X, Y, t) \qquad \text{...(23)}$$

where the displacement of the impactor and the deflection of the panel are designated as $\bar{S}(t)$ and $\bar{W}(X, Y, t)$, respectively. Then, the motion equation of the impactor can be written as follows:

$$m^i \ddot{\bar{S}}(t) + P_c(t) = 0, \quad \bar{S}(0) = 0, \quad \dot{\bar{S}}(0) = V_0 \qquad \text{...(24)}$$

in which m^i and V_0 represent the mass and the initial velocity of the impactor, respectively.

https://doi.org/10.1017/aer.2018.104 Published online by Cambridge University Press

4.0 SOLUTION PROCEDURE

With γ_{ijk} being defined as in Ref. 27, the following dimensionless variables are presented for the sake of solution process convenience

$$x=\pi\frac{X}{a},\quad y=\pi\frac{Y}{b},\quad \beta=\frac{a}{b},\quad \eta=\frac{\pi^2R}{a^2}\left[D_{11}^*D_{22}^*A_{11}^*A_{22}^*\right]^{1/4},$$

$$W=\frac{\overline{W}}{\left[D_{11}^*D_{22}^*A_{11}^*A_{22}^*\right]^{1/4}},\quad F=\frac{\overline{F}}{\left[D_{11}^*D_{22}^*\right]^{1/2}},\quad S=\frac{\overline{S}}{\left[D_{11}^*D_{22}^*A_{11}^*A_{22}^*\right]^{1/4}},$$

$$(\Psi_x,\Psi_y)=\frac{a}{\pi}\frac{(\overline{\Psi}_x,\overline{\Psi}_y)}{\left[D_{11}^*D_{22}^*A_{11}^*A_{22}^*\right]^{1/4}},\quad \gamma_{14}=\left[\frac{D_{22}^*}{D_{11}^*}\right]^{1/2},\quad \gamma_{24}=\left[\frac{A_{11}^*}{A_{22}^*}\right]^{1/2},$$

$$\gamma_5=-\frac{A_{12}^*}{A_{22}^*},\quad (\gamma_{T1},\gamma_{T2})=\left(A_x^T,A_y^T\right)R\left[\frac{A_{11}^*A_{22}^*}{D_{11}^*D_{22}^*}\right]^{1/4},$$

$$v_0=\frac{V_0a}{\pi\left[D_{11}^*D_{22}^*A_{11}^*A_{22}^*\right]^{1/4}}\sqrt{\frac{\rho_0}{E_0}},$$

$$(\gamma_{T3},\gamma_{T4},\gamma_{T6},\gamma_{T7})=\frac{a^2}{\pi^2hD_{11}^*}\left(D_x^T,D_y^T,\frac{4}{3h^2}F_x^T,\frac{4}{3h^2}F_y^T\right),\quad t=\frac{\pi\bar{t}}{a}\sqrt{\frac{E_0}{\rho_0}},$$

$$(M_x,P_x)=\frac{a^2}{\pi^2}\frac{1}{D_{11}^*\left[D_{11}^*D_{22}^*A_{11}^*A_{22}^*\right]^{1/4}}\left(\overline{M}_x,\frac{4}{3h^2}\overline{P}_x\right),$$

$$\lambda_q=\frac{P_ca^4}{\pi^2D_{11}^*\left[D_{11}^*D_{22}^*A_{11}^*A_{22}^*\right]^{1/4}},\quad \gamma_{170}=-\frac{I_1E_0a^2}{\pi^2\rho_0D_{11}^*},\quad (\lambda_x,\lambda_y)=\frac{\left(\sigma_x\pi^2R^2,\sigma_ya^2\right)h}{4\pi^2\left[D_{11}^*D_{22}^*\right]^{1/2}},$$

$$(\gamma_{91},\gamma_{92},\gamma_{81},\gamma_{82},\gamma_{83},\gamma_{84},\gamma_{171},\gamma_{172})=\left(-\hat{I}_3,-\widehat{I}_3',-\widetilde{I}_5,-\widetilde{I}_5',\hat{I}_5,\widehat{I}_5',-\tilde{I}_7,-\widetilde{I}_7'\right)\frac{E_0}{\rho_0D_{11}^*}\qquad ...(25)$$

where ρ_0 and E_0 are the reference values of the CNTRC matrix density and Young's moduli at the room temperature ($T_0=300$ K), and A_x^T, A_y^T, D_x^T, D_y^T, F_x^T and F_y^T are defined as

$$\begin{bmatrix}A_x^T & D_x^T & F_x^T\\ A_y^T & D_y^T & F_y^T\end{bmatrix}\Delta T=-\sum_{k=1}^{}\int_{t_{k-1}}^{t_k}\begin{bmatrix}A_x\\ A_y\end{bmatrix}_k\left(1,Z,Z^3\right)\Delta T\mathrm{d}Z\qquad ...(26)$$

where A_x and A_y is defined in Equation (7).

Then, the non-linear Equations (1)–(4) can be rewritten in the dimensionless form as follows:

$$L_{11}(W)-L_{12}(\Psi_x)-L_{13}(\Psi_y)+\gamma_{14}L_{14}(F)-L_{16}(M^T)-\eta^{-1}\gamma_{14}F_{,xx}=$$
$$\gamma_{14}\beta^2L(W,F)+L_{17}(\ddot{W})+\left(\gamma_{81}\frac{\partial\ddot{\Psi}_x}{\partial x}+\gamma_{82}\beta\frac{\partial\ddot{\Psi}_y}{\partial y}\right)+\lambda_q\qquad ...(27)$$

https://doi.org/10.1017/aer.2018.104 Published online by Cambridge University Press

$$L_{21}(F)+\gamma_{24}L_{22}(\Psi_x)+\gamma_{24}L_{23}(\Psi_y)-\gamma_{24}L_{24}(W)+\eta^{-1}\gamma_{24}W_{,xx}=-\frac{1}{2}\gamma_{24}\beta^2L(W,W) \quad ...(28)$$

$$L_{31}(W)+L_{32}(\Psi_x)-L_{33}(\Psi_y)+\gamma_{14}L_{34}(F)-L_{36}(S^T)=\gamma_{83}\frac{\partial\ddot{W}}{\partial x}+\gamma_{91}\ddot{\Psi}_x \quad ...(29)$$

$$L_{41}(W)-L_{42}(\Psi_x)+L_{43}(\Psi_y)+\gamma_{14}L_{44}(F)-L_{46}(S^T)=\gamma_{84}\beta\frac{\partial\ddot{W}}{\partial y}+\gamma_{92}\ddot{\Psi}_y \quad ...(30)$$

where the dimensionless operators $L_{ij}()$ and $L()$ are defined in[27].

The boundary conditions presented in Equation (14) will be as follows:

$$x=0,\pi:$$

$$W=\psi_y=0 \quad ...(31a)$$

$$M_x=P_x=0 \quad ...(31b)$$

$$\int_0^{\pi}\frac{\partial^2F}{\partial y^2}\mathrm{d}y=0 \text{ (movable)} \quad ...(31c)$$

$$\int_0^{\pi}\int_0^{\pi}\left[\left(\gamma_{24}^2\beta^2\frac{\partial^2F}{\partial y^2}-\gamma_5\frac{\partial^2F}{\partial x^2}\right)+\gamma_{24}\left(\gamma_{511}\frac{\partial\Psi_x}{\partial x}+\gamma_{233}\beta\frac{\partial\Psi_y}{\partial y}\right)\right.$$
$$-\gamma_{24}\left(\gamma_{611}\frac{\partial^2W}{\partial x^2}+\gamma_{244}\beta^2\frac{\partial^2W}{\partial y^2}\right)-\frac{1}{2}\gamma_{24}\left(\frac{\partial W}{\partial x}\right)^2$$
$$\left.+\eta^{-1}\left(\gamma_{24}^2\gamma_{T1}-\gamma_5\gamma_{T2}\right)\right]\Delta T\mathrm{d}x\mathrm{d}y=0 \text{ (immovable)} \quad ...(31d)$$

$$y=0,\pi:$$

$$W=\Psi_x=0 \quad ...(31e)$$

$$M_y=P_y=0 \quad ...(31f)$$

$$\int_0^{\pi}\frac{\partial^2F}{\partial x^2}\mathrm{d}y=0 \text{ (movable)} \quad ...(31g)$$

$$\int_0^{\pi}\int_0^{\pi}\left[\left(\frac{\partial^2F}{\partial x^2}-\gamma_5\beta^2\frac{\partial^2F}{\partial y^2}\right)+\gamma_{24}\left(\gamma_{220}\frac{\partial\Psi_x}{\partial x}+\gamma_{522}\beta\frac{\partial\Psi_y}{\partial y}\right)\right.$$
$$-\gamma_{24}\left(\gamma_{240}\frac{\partial^2W}{\partial x^2}+\gamma_{622}\beta\frac{\partial^2W}{\partial y^2}\right)+\eta^{-1}\gamma_{24}W-\frac{1}{2}\gamma_{24}\beta^2\left(\frac{\partial W}{\partial y}\right)^2$$
$$\left.+\eta^{-1}\left(\gamma_{T2}-\gamma_5\gamma_{T1}\right)\right]\mathrm{d}y\mathrm{d}x=0 \text{ (immovable)} \quad ...(31h)$$

https://doi.org/10.1017/aer.2018.104 Published online by Cambridge University Press

Mathematically, Equations (27)–(30) can be divided into two sets and solved sequentially. The first set of equations forms the solution of static deflection because of thermal bending moments, and the second one yields the homogeneous solution of vibration on the initially deflected panel. Using a two-step perturbation technique[9], the solution for the second set of equations can be expressed as

$$W(x,y,t)=\epsilon A_{11}^{(1)}(t)\sin(mx)\sin(ny)+\left(\epsilon A_{11}^{(1)}(t)\right)^3[\alpha_{331}\sin(3mx)\sin(ny)+\alpha_{313}\sin(mx)\sin(3ny)]+Q(\epsilon^4) \quad ...(32)$$

$$\Psi_x(x,y,t)=\left[\left(\epsilon A_{11}^{(1)}(t)\right)c_{111}+\left(\epsilon \ddot{A}_{11}^{(1)}(t)\right)c_{311}\right]\cos(mx)\sin(ny)+\left(\epsilon A_{11}^{(1)}(t)\right)^3[c_{331}\cos(3mx)\sin(ny)+c_{313}\cos(mx)\sin(3ny)]+O(\epsilon^4) \quad ...(33)$$

$$\Psi_y(x,y,t)=\left[\left(\epsilon A_{11}^{(1)}(t)\right)d_{111}+\left(\epsilon \ddot{A}_{11}^{(1)}(t)\right)d_{311}\right]\sin(mx)\cos(ny)+\left(\epsilon A_{11}^{(1)}(t)\right)^3[d_{331}\sin(3mx)\cos(ny)+d_{313}\sin(mx)\cos(3ny)]+O(\epsilon^4) \quad ...(34)$$

$$F(x,y,t)=-B_{00}^{(0)}y^2/2-b_{00}^{(0)}x^2/2+\left[\left(\epsilon A_{11}^{(1)}(t)\right)\beta_{111}+\left(\epsilon \ddot{A}_{11}^{(1)}(t)\right)\beta_{311}\right]\times\sin(mx)\sin(ny)+\left(\epsilon A_{11}^{(1)}(t)\right)^2\left[-B_{00}^{(2)}y^2/2-b_{00}^{(2)}x^2/2+\beta_{202}\cos(2ny)+\beta_{220}\cos(2mx)\right]+\left(\epsilon A_{11}^{(1)}(t)\right)^3[\beta_{331}\sin(3mx)\sin(ny)+\beta_{313}\sin(mx)\sin(3ny)]+O(\epsilon^4) \quad ...(35)$$

$$\lambda_q(x,y,t)=\left[\left(\epsilon \ddot{A}_{11}^{(1)}(t)\right)g_{30}+\left(\epsilon A_{11}^{(1)}(t)\right)g_{31}\right]\sin(mx)\sin(ny)+\left(\epsilon A_{11}^{(1)}(t)\right)^2[g_{220}\cos(2mx)+g_{202}\cos(2ny)]+\left(\epsilon A_{11}^{(1)}(t)\right)^3[g_{33}\sin(mx)\sin(ny)]+\cdots \quad ...(36)$$

where $\left(\epsilon A_{11}^{(1)}(t)\right)$ is the second perturbation parameter which is related to the dimensionless vibration amplitude.

The non-linear equations of motion of both panel and impactor in the loading phase can be determined by setting $(x,y)=(\pi/2,\pi/2)$ in Equation (36):

$$\sin\left(\frac{m\pi}{2}\right)\sin\left(\frac{n\pi}{2}\right)\left[g_{30}\frac{d^2\left(\epsilon A_{11}^{(1)}(t)\right)}{dt^2}+g_{31}\left(\epsilon A_{11}^{(1)}(t)\right)\right]+\left(\epsilon A_{11}^{(1)}(t)\right)^2\times[g_{220}\cos(m\pi)+g_{202}\cos(n\pi)]+\left(\epsilon A_{11}^{(1)}(t)\right)^3\left[g_{33}\sin\left(\frac{m\pi}{2}\right)\sin\left(\frac{n\pi}{2}\right)\right]=g_{34}\left[S(t)-\sin\left(\frac{m\pi}{2}\right)\sin\left(\frac{n\pi}{2}\right)\left(\epsilon A_{11}^{(1)}\right)-\left(\epsilon A_{11}^{(1)}\right)^3\left[\alpha_{331}\sin\left(\frac{3m\pi}{2}\right)\sin\left(\frac{n\pi}{2}\right)+\alpha_{313}\sin\left(\frac{m\pi}{2}\right)\sin\left(\frac{3n\pi}{2}\right)\right]\right]^{1.5} \quad ...(37)$$

https://doi.org/10.1017/aer.2018.104 Published online by Cambridge University Press

$$\frac{d^2(S(t))}{dt^2} = -g_{35}\left[S(t) - \sin\left(\frac{m\pi}{2}\right)\sin\left(\frac{n\pi}{2}\right)\left(\epsilon A_{11}^{(1)}\right) - \left(\epsilon A_{11}^{(1)}\right)^3\left[\alpha_{331}\sin\left(\frac{3m\pi}{2}\right)\sin\left(\frac{n\pi}{2}\right) + \alpha_{313}\sin\left(\frac{m\pi}{2}\right)\sin\left(\frac{3n\pi}{2}\right)\right]\right]^{1.5} \quad ...(38)$$

The symbols used in Equations (37) and (38) are given in Appendix A. Satisfying the convenient initial conditions (i.e. $\epsilon A_{11}^{(1)}(0) = \epsilon A_{11}^{(1)}(0) = S(0) = 0,\ S(0) = v_0$) Equations (38) and (39) can be solved using the Runge–Kutta iteration method. By substituting the solution into Equations (32)–(36), the displacements and contact force of the shell can be obtained.

5.0 NUMERICAL RESULTS AND DISCUSSION

In this section, numerical results are presented for sandwich cylindrical panels with CNTML face sheets subjected to transverse low-velocity impact in various thermal environments. As mentioned before, there is no study neither on the low-velocity impact response of sandwich nor CNTML and FG-CNTRC cylindrical panels. In this study, the non-linear temperature-dependent low-velocity impact response of nanotube-reinforced composite cylindrical panel-type structures is studied. For verification of the employed method, the problem of a simply supported square isotropic steel plate subjected to low-velocity impact with a steel spherical indenter with the following material and geometrical information previously treated by Refs 33–36 is resolved:

- Plate: $E = 206.8$ GPa, $\nu = 0.3$, $\rho = 7810$ kg/m^3, length $a = b = 200$ mm and thickness $h = 8$ mm
- Impactor: $E = 206.8$ GPa, $\nu = 0.3$, $\rho = 7810$ kg/m^3, diameter $D_i = 20$ mm and velocity $V_0 = 1$ m/s

Time histories of the impactor displacement and contact force found using the present method are shown in Figs 2 and 3, respectively. Present results are compared with those reported by Karas[33], Wu and Chung[34], Khalili et al.[35] and Wu and Springer[36]. The results of the present model are in a good agreement with existing ones. The little negligible difference between presented results and some existing one[35] may be due to the use of classical plate theory and linearised contact law; while higher-order shear deformation theory and a non-linear contact law are used in present study.

First of all, the effective material properties of CNTRCs are needed to be determined. Ploy methyl methacrylate, labelled as PMMA, is chosen for the matrix with material properties of $\rho^m = 1150$ kg/m^3, $\nu^m = 0.34$, $\alpha^m = 45(1 + 0.0005\Delta T) \times 10^{-6}$/K and $E^m = (3.52 - 0.0034T)$ GPa, where $T = T_0 + \Delta T$ and $T_0 = 300$ K (room temperature). In this way, $\alpha^m = 45.0 \times 10^{-6}$/K and $E^m = 2.5$ GPa at $T = 300$ K. The (10,10) single-walled carbon nanotubes (SWCNTs) are chosen as reinforcements. As listed in Table 1, typical size and temperature-dependent material properties of CNTs are obtained using MD simulations[37]. It should be mentioned that the manufacturing procedure of (10,10) SWCNTs are described in detail in Ref. 38.

Aluminium 2024-T3 is selected for the metal part of CNTML, with temperature-dependent material properties given in Table 2[39]. To comprehensively define a CNTML laminate, the following coding system is used. The coding system of nanotube-reinforced aluminium laminate is Al/CNT $(1 + i)/i$, for instance, for $i = 3$, Al/CNT 4/3 defines a laminate composed of four aluminium and three nanotube-reinforced layers stacked together (i.e. Al/CNT/Al/

https://doi.org/10.1017/aer.2018.104 Published online by Cambridge University Press

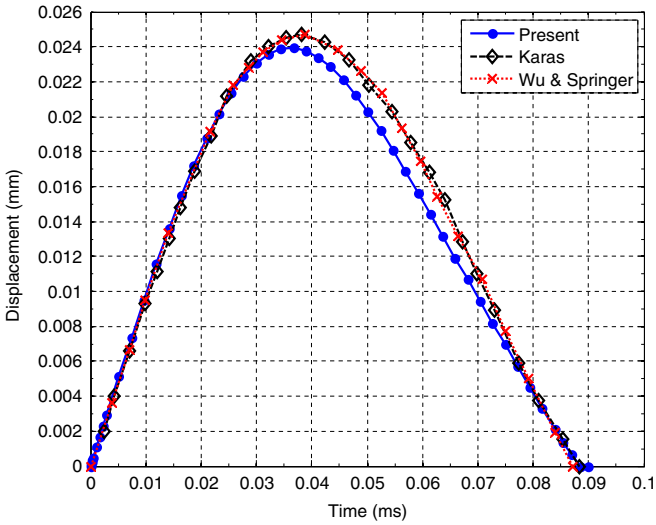

Figure 2. Time history of impactor displacement of an isotropic plate subjected to low-velocity impact predicted by Karas[33], Wu and Springer[36] and present method.

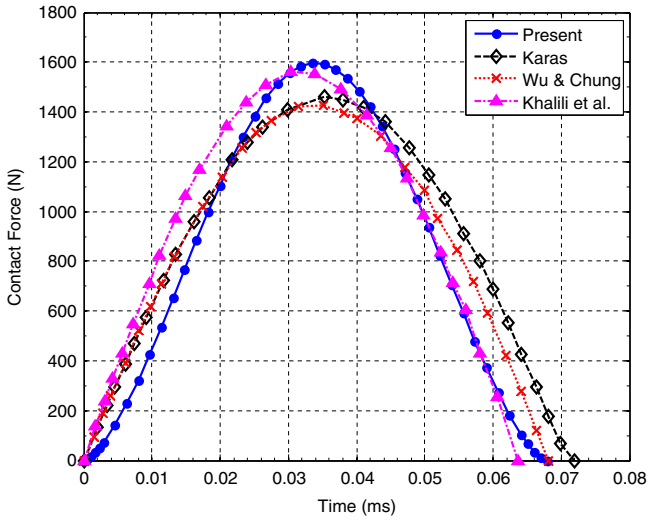

Figure 3. Time history of contact force of isotropic plate subjected to low-velocity impact predicted by Karas[33], Wu and Chung[34], Khalili et al.[35] and present method.

CNT/Al/CNT/AL). In the following examples, the thickness of metal and CNTRC layers are assumed to be $h_{Al} = 0.2$ mm and $h_{CNT} = 0.3$ mm, respectively.

The CNT efficiency parameters η_i $(i = 1,2,3)$ are crucial in the successful application of the extended rule of mixture to CNTRCs. Unfortunately, no experiments have been done to determine the values of η_i for CNTRCs, yet. As it was mentioned before, these parameters can be calculated by matching theoretical results of extended rule of mixture to those of experiments or MD simulations. In this study, the longitudinal and transverse Young's moduli and in-plane shear moduli of CNTs obtained from MD simulations given by Han and Elliott[4]

https://doi.org/10.1017/aer.2018.104 Published online by Cambridge University Press

Table 1
Temperature-dependent material properties for (10,10) SWCNT
($L = 9.26$ nm, $R = 0.68$ nm, $h = 0.067$ nm and ν_{12}^{CN}=0.175)

Temperature (K)	E_{11}^{CN}(TPa)	E_{22}^{CN}(TPa)	G_{12}^{CN}(TPa)	$\alpha_{11}^{CN}(\times 10^{-6}/\mathrm{K})$	$\alpha_{22}^{CN}(\times 10^{-6}/\mathrm{K})$
300	5.6466	7.0800	1.9445	3.4584	5.1682
400	5.5679	6.9814	1.9703	4.1496	5.0905
500	5.5308	6.9348	1.9643	4.5361	5.0189
700	5.4744	6.8641	1.9644	4.6677	4.8943

Table 2
Temperature-dependent material properties of aluminium 2024-T3
($\nu = 0.33$ and $\rho = 2770\ \mathrm{kg/m^3}$)[39]

Temperature (K)	E (GPa)	α ($\times 10^{-6}$/K)
300	73.4	22.5
400	68.6	24.3
500	64.2	25.5

are matched to those predicted from the extended rule of mixture in order to estimate the CNT efficiency parameters. As previously presented in Ref. 37, these parameters are listed in Table 3. In the following examples, these values are used in which it is assumed that $G_{13} = G_{12}$ and $G_{23} = 1.2G_{12}$[40].

Three types of FG-CNTRC layers (i.e. FG-Λ, FG-V and FG-X) are considered. A UD-CNTRC layer is also considered for comparison. Also, the deflected mode is assumed to be $(m,n) = (1,1)$. The impactor is made of steel ($\rho^{i} = 7960\ \mathrm{kg/m^3}$, $E^{i} = 207$ GPa and $\nu^{i} = 0.3$) with a radius of $R = 6.35$ mm and an initial velocity of $V_0 = 3$ m/s.

The low-velocity impact response of sandwich cylindrical panels with Al/CNT 2/1 face sheets and FG-X core is presented in this section. For all cases below, the cylindrical panel geometric parameters are taken as $a = b = 200$ mm and $R/a = 5$. The Al/CNT 2/1 is selected for sandwich panel face sheets. Also, the CNT layer is assumed to be FG of type X, due to its high strength to impact[41]. Titanium alloy, referred to as Ti–6Al–4V, and Zirconia are selected as metal and ceramic part of FG core, respectively; the material properties of which are given in Table 4 as a non-linear function of temperature[42]. The thickness of homogeneous or FG core is taken to be $h_c = 4$, 6 and 8 mm.

Table 3
(10,10) SWCNT efficiency parameters ($L = 9.26$ nm, $R = 0.68$ nm,
$h = 0.067$ nm and ν_{12}^{CN}=0.175)

V_{CN}^{*}	η_1	η_2	η_3
0.12	0.137	1.022	0.715
0.17	0.142	1.626	1.138
0.28	0.141	1.585	1.109

https://doi.org/10.1017/aer.2018.104 Published online by Cambridge University Press

Table 4
Material property of the constituent materials of the considered FG core as a non-linear function of temperature ($P = P_0(P_{-1}/T + 1 + P_1T + P_2T^2 + P_3T^3)$)[42]

Material	Property	P_0	P_{-1}	P_1	P_2	P_3
Ti–6Al–4V	E (Pa)	$122.55676e^9$	0	$-4.58635e^{-4}$	0	0
	ν	0.28838235	0	$1.12136e^{-4}$	0	0
	α (per K)	$7.57876e^{-6}$	0	0.00065	$0.31467e^{-6}$	0
	ρ (kg/m^3)	4429	0	0	0	0
Zirconia	E (Pa)	$244.26596e^9$	0	$-1.3707e^{-3}$	$1.21393e^{-6}$	$-3.681378e^{-10}$
	ν	0.2882	0	$1.13345e^{-4}$	0	0
	α (per K)	$12.7657e^{-6}$	0	−0.00149	$1e^{-6}$	$-0.6775e^{-11}$
	ρ (kg/m^3)	5700	0	0	0	0

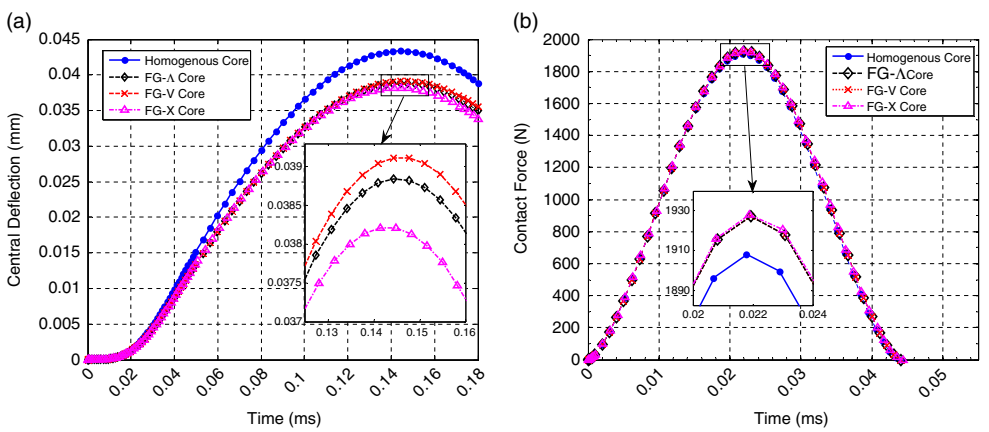

Figure 4. Comparison of the impact response of sandwich cylindrical panels with four types of cores: (a) central deflection and (b) contact force ($a/b = 1$, $a = 200$ mm, $R/a = 5$, $h_{Al} = 0.2$ mm, $h_{CNT} = 0.3$ mm, $h_{core} = 6$ mm, $n = 1$, $V^*_{CN} = 0.17$, $V_0 = 3$ m/s and $T = 300$ K).

Low-velocity impact response of sandwich cylindrical panels with Al/CNT 2/1 face sheets and four types of core (i.e. homogenous, FG-Λ, FG-V and FG-X) is displayed in Fig. 4. The panel with FG-X core has the lowest central deflection while the contact forces are almost the same. Also the power index of the FG core, mentioned in Equation (14), can influence the impact response of the sandwich panels with FG cores. Therefore, the impact response of sandwich panels with FG core of type X with five various power indexes is compared in Fig. 5. Using a power index of $n = 0.1$ significantly decreases the central deflection, however, slightly increases the contact force. Hence, the FG core of type X with power index of $n = 0.1$ will be considered in the following examples.

The effect of core thickness on the low-velocity impact response of the sandwich cylindrical panel with Al/CNT 2/1 face sheets with CNT volume fraction of $V^*_{CN} = 0.12$ and FG-X core with power index of $n = 0.1$ is presented in Fig. 6. The sandwich panel with thicker core has lower central deflection along with a little higher contact force.

https://doi.org/10.1017/aer.2018.104 Published online by Cambridge University Press

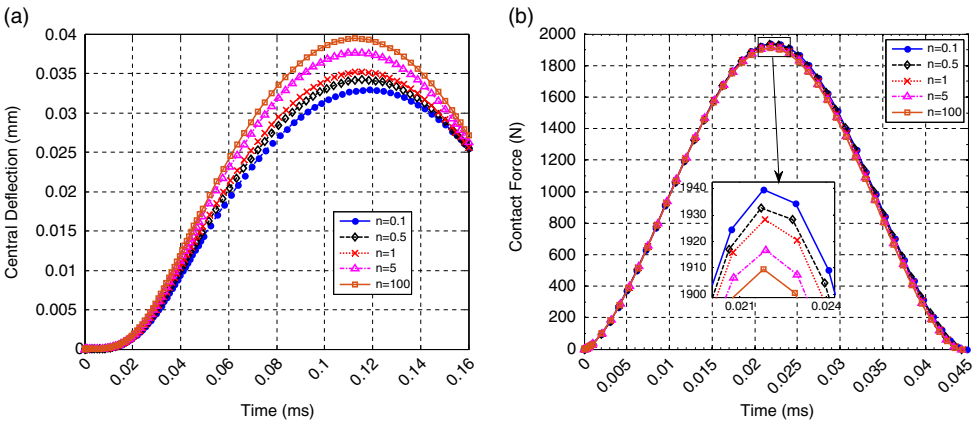

Figure 5. The effect of power index of FG core of sandwich panel on the impact response: (a) central deflection and (b) contact force ($a/b=1$, $a=200$ mm, $R/a=5$, $h_{Al}=0.2$ mm, $h_{CNT}=0.3$ mm, $h_{core}=6$ mm, $V^*_{CN}=0.17$, $V_0=3$ m/s and $T=300$ K).

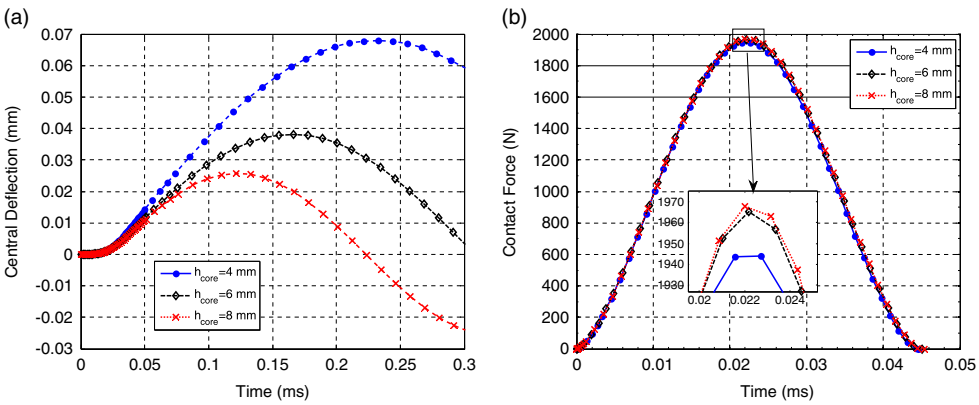

Figure 6. The effect of core thickness on low-velocity impact response of sandwich cylindrical panel with Al/CNT 2/1 face sheets and FG-X core: (a) central deflection and (b) contact force ($a/b=1$, $a=200$ mm, $R/a=5$, $h_{Al}=0.2$ mm, $h_{CNT}=0.3$ mm, $n=0.1$, $V^*_{CN}=0.12$, $V_0=3$ m/s and $T=300$ K).

The low-velocity impact response of sandwich cylindrical panels with various CNT volume fractions is illustrated in Fig. 7. The sandwich panels with higher CNT volume fraction in their CNTML face sheets respond faster to the low-velocity impact than others (i.e. reach to their maximum of central deflection faster) which can be due to their stiffer CNTRC layer. Also, the sandwich panel with the CNT volume fraction of $V^*_{CN}=0.17$ of its CNTML face sheet has the lowest central deflection in comparison with others. There is no considerable change in contact force of sandwich panels with three different CNT volume fractions; however, as the CNT volume fraction increases, the contact force decreases slightly.

The effect of impactor initial velocity on the low-velocity impact response of sandwich cylindrical panel is presented in Fig. 8. Similar to single-layer CNTRC and CNTML cylindrical panels, the central deflection as well as the contact force of the sandwich panel increases as the impactor initial velocity increases. However, this example can be

https://doi.org/10.1017/aer.2018.104 Published online by Cambridge University Press

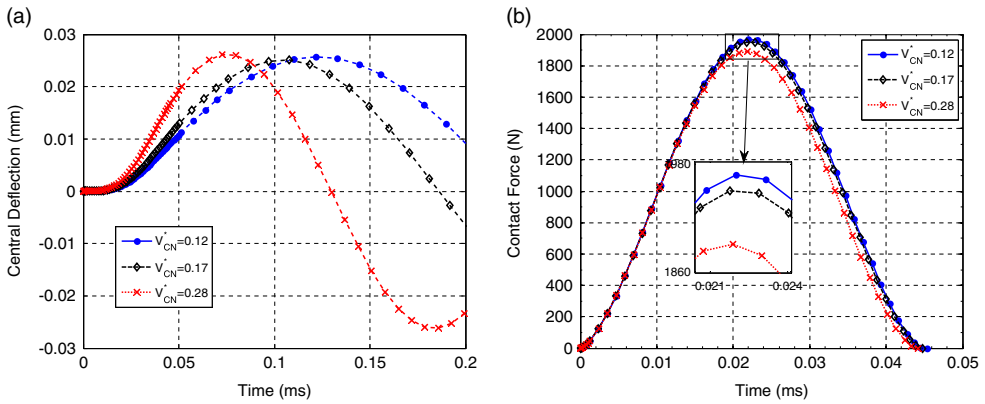

Figure 7. The effect of CNT volume fraction on low-velocity impact response of sandwich cylindrical panel with Al/CNT 2/1 face sheets and FG-X core: (a) central deflection and (b) contact force ($a/b = 1$, $a = 200$ mm, $R/a = 5$, $h_{Al} = 0.2$ mm, $h_{CNT} = 0.3$ mm, $h_{core} = 8$ mm, $n = 0.1$, $V_0 = 3$ m/s and $T = 300$ K).

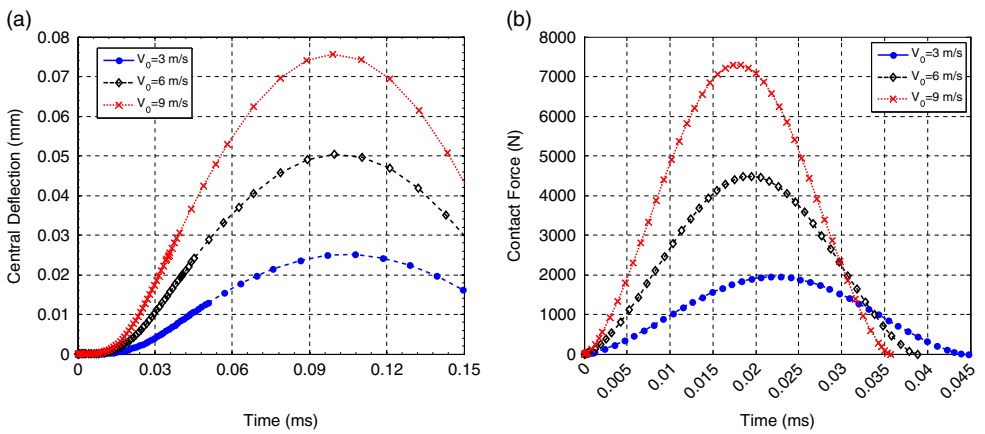

Figure 8. The effect of impactor initial velocity on low-velocity impact response of sandwich cylindrical panel with Al/CNT 2/1 face sheets and FG-X core: (a) central deflection and (b) contact force ($a/b = 1$, $a = 200$ mm, $R/a = 5$, $h_{Al} = 0.2$ mm, $h_{CNT} = 0.3$ mm, $h_{core} = 8$ mm, $n = 0.1$, $V^*_{CN} = 0.17$ and $T = 300$ K).

quantitatively helpful in optimally designing sandwich cylindrical panels with CNTML face sheets and FG core.

The effect of temperature on the low-velocity impact response of the sandwich cylindrical panels with 'immovable' edge boundary conditions is also illustrated in Fig. 9. The central deflection increases significantly in elevated temperature because of 'immovable' boundary condition and thermal effects. However, the contact force changes negligibly.

To see the effect of boundary condition, the impact response of sandwich panels with two types of boundary conditions (i.e. 'movable' and 'immovable') is presented in Fig. 10. Obviously, the central deflection increases considerably when the edge boundary condition is 'immovable'. As was discussed previously, there is no change in the contact force when the edge boundary condition changes to 'immovable'.

https://doi.org/10.1017/aer.2018.104 Published online by Cambridge University Press

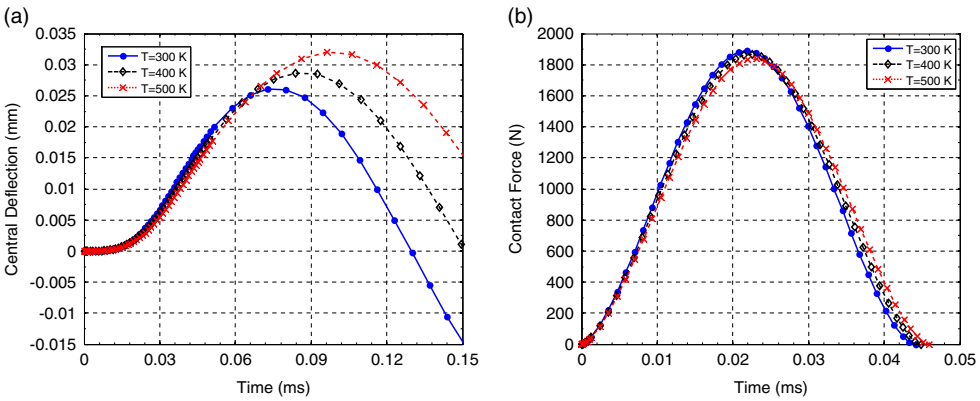

Figure 9. Low-velocity impact response of sandwich cylindrical panel with Al/CNT 2/1 face sheets and FG-X core in various thermal environments and with 'immovable' edge boundary condition: (a) central deflection and (b) contact force ($a/b=1$, $a=200$ mm, $R/a=5$, $h_{Al}=0.2$ mm, $h_{CNT}=0.3$ mm, $h_{core}=8$ mm, $n=0.1$, $V^*_{CN}=0.28$ and $V_0=3$ m/s).

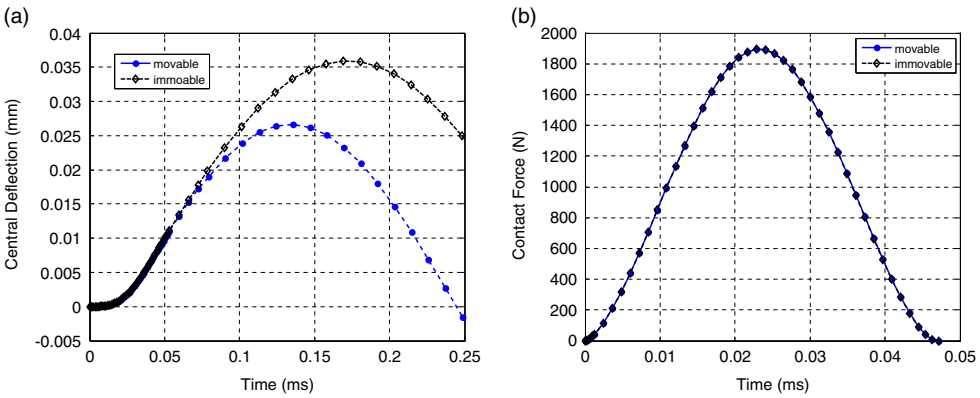

Figure 10. The effect of edge boundary condition on low-velocity impact response of sandwich cylindrical panel with Al/CNT 2/1 face sheets and FG-X core: (a) central deflection and (b) contact force ($a/b=1$, $a=200$ mm, $R/a=5$, $h_{Al}=0.2$ mm, $h_{CNT}=0.3$ mm, $h_{core}=8$ mm, $V^*_{CN}=0.12$, $V_0=3$ m/s and $T=500$ K).

6.0 SUMMARY AND CONCLUSION

The non-linear low-velocity impact response of sandwich cylindrical panels with CNTRC and metal face sheets and four types of core (i.e. homogenous, FG-Λ, FG-V and FG-X) in thermal environments was presented. The present method was validated with the existing literature data. A parametric study of various effective parameters on the impact response was conducted. The presented numerical examples demonstrate that the CNT volume fraction, impactor initial velocity and the thermal environment have a significant role on the impact response of CNTRC cylindrical panels. In addition, the effect of geometrical parameters was studied. It was found that functionally grading the CNTRC core with the power index of

https://doi.org/10.1017/aer.2018.104 Published online by Cambridge University Press

$n = 0.1$, significantly decreases the central deflection, however, slightly increases the contact force. Also, the sandwich panel with thicker core has been discovered to have lower central deflection along with a little higher contact force. Moreover, the sandwich panels with higher CNT volume fraction in their CNTML face sheets are found to respond faster to the low-velocity impact than others. The presented analysis and numerical results can be useful in optimally designing nanocomposite structures subjected to impact in thermal environments.

APPENDIX A

In Equations (37) and (38)

$$\theta_2 = \frac{1}{2}\left[\frac{3g_{33}}{4g_{31}} - \frac{5g_{32}^2}{6g_{31}^2}\right], \quad \theta_4 = \frac{1}{2}\left[\frac{5g_{35}}{8g_{31}} - \frac{15g_{33}^2}{128g_{31}^2} + \frac{13g_{32}^2 g_{33}}{32g_{31}^3} - \frac{491g_{32}^4}{864g_{31}^4}\right],$$

$$g_{30} = -\left[\gamma_{170} - \left(\gamma_{171}m^2 + \gamma_{172}n^2\beta^2\right)\right] - \frac{\gamma_{81}m^2 g_{04} + \gamma_{82}n^2\beta^2 g_{03}}{g_{00}}$$

$$+ \gamma_{14}\gamma_{24}\frac{g_{05}^*}{g_{06}}\frac{\gamma_{81}m^2 g_{02} + \gamma_{82}n^2\beta^2 g_{01}}{g_{00}} - g_{08}^* - \gamma_{14}\gamma_{24}\frac{g_{07}^* g_{05}^{**}}{g_{06}}, \quad g_{31} = Q_{11} - D_{02},$$

$$g_{32} = -\frac{2}{3\pi^2 mn}\gamma_{14}\gamma_{24}m^2n^2\beta^2\left(\frac{\gamma_8}{\gamma_6} + \frac{\gamma_9}{\gamma_7} + \frac{1}{4m^2\eta\gamma_6} + 4\frac{g_{05}^*}{g_{06}}\right)$$

$$(1-\cos(m\pi))(1-\cos(n\pi)) + 2g_{33}\Phi(T), \quad g_{33} = \frac{1}{16}\gamma_{14}\gamma_{24}\left(\frac{m^4}{\gamma_7} + \frac{n^4\beta^4}{\gamma_6}\right) - D_{22},$$

$$(g_{34}, g_{35}) = \left(\frac{K_c a^2}{\pi^2 D_{11}^*}, -\frac{K_c a^2\rho_0}{m^i\pi^2 E_0}\right)\left[D_{11}^* D_{22}^* A_{11}^* A_{22}^*\right]^{1/8}$$

$$g_{220} = \gamma_{14}\gamma_{24}n^2\beta^2\left(\frac{4m^2\gamma_8 + \eta^{-1}}{8\gamma_6} + m^2\frac{g_{05}^*}{g_{06}}\right),$$

$$g_{202} = \gamma_{14}\gamma_{24}m^2n^2\beta^2\left(\frac{1}{2}\frac{\gamma_9}{\gamma_7} + \frac{g_{05}^*}{g_{06}}\right) \qquad \ldots(A.1)$$

in which (with other symbols given as in Refs 43,45)

$$Q_{11} = g_{08} + \gamma_{14}\gamma_{24}\frac{g_{05}^* g_{07}^*}{g_{06}},$$

$$D_{02} = \gamma_{14}\left(B_{00}^{(0)}m^2 + b_{00}^{(0)}n^2\beta^2\right), \quad D_{22} = \gamma_{14}\left(B_{00}^{(2)}m^2 + b_{00}^{(2)}n^2\beta^2\right),$$

$$\Phi(T) = \lambda + \Theta_2(\lambda)^2 + \Theta_3(\lambda)^3 + \cdots \qquad \ldots(A.2)$$

also

$$\Phi(T) = \lambda + \Theta_2(\lambda)^2 + \Theta_3(\lambda)^3 + \cdots \qquad \ldots(A.3)$$

https://doi.org/10.1017/aer.2018.104 Published online by Cambridge University Press

where

$$\lambda = \frac{16}{\pi^2 G_{08}}\left(\left(\gamma_{T3}m^2+\gamma_{T4}n^2\beta^2\right)-\frac{(\gamma_{T3}-\gamma_{T6})m^2 g_{102}+(\gamma_{T4}-\gamma_{T7})n^2\beta^2 g_{101}}{g_{00}}\right)\Delta T \times \frac{h}{\left[D_{11}^* D_{22}^* A_{11}^* A_{22}^*\right]^{1/4}},$$

$$\Theta_2 = \frac{8}{3\pi^2 G_{08}}\gamma_{14}\gamma_{24}m^2n^2\beta^2\left(\frac{\gamma_8}{\gamma_6}+\frac{\gamma_9}{\gamma_7}+\frac{1}{4m^2\eta\gamma_6}+4\frac{g_{05}^*}{g_{06}}\right),$$

$$\Theta_3 = 2\Theta_2^2-\frac{g_{33}}{Q_{11}-D_{02}} \quad ...(A.4)$$

For 'movable' edge boundary condition

$$B_{00}^{(0)} = B_{00}^{(2)} = b_{00}^{(0)} = b_{00}^{(2)} = 0, \quad ...(A.5)$$

and for 'immovable' edge boundary condition

$$B_{00}^{(0)} = \eta^{-1}\gamma_{T1}\Delta T, \quad B_{00}^{(2)} = -\frac{1}{8}\gamma_{24}\frac{m^2+\gamma_5 n^2\beta^2}{\gamma_{24}^2-\gamma_5^2},$$

$$b_{00}^{(0)} = \eta^{-1}\gamma_{T2}\Delta T, \quad b_{00}^{(2)} = -\frac{1}{8}\gamma_{24}\frac{\gamma_5 m^2+\gamma_{24}^2 n^2\beta^2}{\gamma_{24}^2-\gamma_5^2}. \quad ...(A.6)$$

REFERENCES

1. COLEMAN, J.N., KHAN, U., BLAU, W.J. and GUN'KO, Y.K. Small but strong: a review of the mechanical properties of carbon nanotube–polymer composites, *Carbon (New York)*, 2006, **44**, pp 1624–1652. https://doi.org/10.1016/j.carbon.2006.02.038.
2. QIAN, D., DICKEY, E., ANDREWS, R. and RANTELL, T. Load transfer and deformation mechanisms in carbon nanotube–polystyrene composites, *Applied Physics Letters*, 2000, **2868**, pp 4–7. https://doi.org/10.1063/1.126500.
3. HAIDER, M.F., MAJUMDAR, P.K., ANGELONI, S. and REIFSNIDER, K.L. Nonlinear anisotropic electrical response of carbon fiber-reinforced polymer composites, *J Composite Material*, 2018, **52**, 1017–1032.
4. HAN, Y. and ELLIOTT, J. Molecular dynamics simulations of the elastic properties of polymer/carbon nanotube composites, *Computer Materials Science*, 2007, **39**, pp 315–323. https://doi.org/10.1016/j.commatsci.2006.06.011.
5. BONNET, P., SIREUDE, D., GARNIER, B. and CHAUVET, O. Thermal properties and percolation in carbon nanotube–polymer composites, *Applied Physics Letters*, 2007, **91**, pp 1–4. https://doi.org/10.1063/1.2813625.
6. MEGUID, S.A. and SUN, Y. On the tensile and shear strength of nano-reinforced composite interfaces, *Material Design*, 2004, **25**, pp 289–296. https://doi.org/10.1016/j.matdes.2003.10.018.
7. SHEN, H.S. Nonlinear bending of functionally graded carbon nanotube-reinforced composite plates in thermal environments, *Composite Structures*, 2009, **91**, pp 9–19. https://doi.org/10.1016/j.compstruct.2009.04.026.
8. KWON, H., BRADBURY, C.R. and LEPAROUX, M. Fabrication of functionally graded carbon nanotube-reinforced aluminum matrix composite, *Advanced Engineering Materials*, 2011, **13**, pp 325–329. https://doi.org/10.1002/adem.201000251.
9. SHEN, H.S. and XIANG, Y. Nonlinear vibration of nanotube-reinforced composite cylindrical panels resting on elastic foundations in thermal environments, *Composite Structures*, 2015, **49**, pp 49–59. https://doi.org/10.1016/j.euromechsol.2014.06.007.

https://doi.org/10.1017/aer.2018.104 Published online by Cambridge University Press

10. DAVALOS, J.F., QIAO, P., FRANK XU, X., ROBINSON, J. and BARTH, K.E. Modeling and characterization of fiber-reinforced plastic honeycomb sandwich panels for highway bridge applications, *Composite Structures*, 2001, **52**, pp 441–452. https://doi.org/10.1016/S0263-8223(01)00034-4.
11. APETRE, N.A., SANKAR, B.V. and AMBUR, D.R. Low-velocity impact response of sandwich beams with functionally graded core, *Int J Solids Structures*, 2006, **43**, pp 2479–2496. https://doi.org/10.1016/j.ijsolstr.2005.06.003.
12. MIYAMOTO, R.G.F.Y., KAYSSER, W.A., RABIN, B.H. and KAWASAKI, A. *Functionally Graded Materials: Design, Processing and Applications*, Springer Science & Business Media, New York, US, 2013.
13. VENKATARAMAN, S. and SANKAR, B.V. Elasticity solution for stresses in a sandwich beam with functionally graded core, *AIAA J*, 2003, **41**, pp 2501–2505. https://doi.org/10.2514/2.6853.
14. VLOT, A.D. and GUNNINK, J.W. *Fibre Metal Laminates: An Introduction*, Springer Science & Business Media, New York, US, 2011. https://doi.org/10.1007/978-94-010-0995-9.
15. VERMEEREN, C.A.J.R. An historic overview of the development of fibre metal laminates, *Appl Compos Mater*, 2003, **10**, pp 189–205. https://doi.org/10.1023/A:1025533701806.
16. ROEBROEKS, G. Fibre–metal laminates: recent developments and applications, *Int J Fatigue*, 1994, **16**, pp 33–42. https://doi.org/10.1016/0142-1123(94)90443-X.
17. VLOT, A. and KRULL, M. Impact damage resistance of various fibre metal laminates, *Le J Physique*, 1997, **IV**. 7, pp C3–1045.
18. TAN, C.Y. and AKIL, H.M. Impact response of fiber metal laminate sandwich composite structure with polypropylene honeycomb core, *Composites Part B: Engineering*, 2012, **43**, pp 1433–1438. https://doi.org/10.1016/j.compositesb.2011.08.036.
19. AKTAŞ, M., ATAS, C., İÇTEN, B.M. and KARAKUZU, R. An experimental investigation of the impact response of composite laminates, *Composites Structures*, 2009, **87**, pp 307–313. https://doi.org/10.1016/j.compstruct.2008.02.003.
20. SALAMI, S.J. Low velocity impact response of sandwich beams with soft cores and carbon nanotube reinforced face sheets based on extended high order sandwich panel theory, *Aerospace Science Technol*, 2017.
21. WANG, J., WAAS, A.M. and WANG, H. Experimental and numerical study on the low-velocity impact behavior of foam-core sandwich panels, *Composites Structures*, 2013, **96**, pp 298–311. https://doi.org/10.1016/j.compstruct.2012.09.002.
22. JAM, J.E. and KIANI, Y. Low velocity impact response of functionally graded carbon nanotube reinforced composite beams in thermal environment, *Composites Structures*, 2015, **132**, pp 35–43. https://doi.org/10.1016/j.compstruct.2015.04.045.
23. WANG, Z.X., XU, J. and QIAO, P. Nonlinear low-velocity impact analysis of temperature-dependent nanotube-reinforced composite plates, *Composites Structures*, 2014, **108**, pp 423–434. https://doi.org/10.1016/j.compstruct.2013.09.024.
24. KIRATISAEVEE, H. Low-velocity impact response of high-performance aluminum foam sandwich structures, *J Reinforced Plastics and Composites*, 2005, **24**, pp 1057–1072. https://doi.org/10.1177/0731684405048205.
25. MEO, M., VIGNJEVIC, R. and MARENGO, G. The response of honeycomb sandwich panels under low-velocity impact loading, *Int J Mechanical Sciences*, 2005, **47**, pp 1301–1325. https://doi.org/10.1016/j.ijmecsci.2005.05.006.
26. REDDY, J.N.N. A refined nonlinear theory of plates with transverse shear deformation, *Int J Solids Structures*, 1984, **20**, pp 881–896. https://doi.org/10.1016/0020-7683(84)90056-8.
27. HUISHEN, S. Kármán-type equations for a higher-order shear deformation plate theory and its use in the thermal postbuckling analysis, *Applied Mathematics and Mechanics*, 1997, **18**, pp 615–621.
28. REDDY, J.N. and LIU, C.F. A higher-order shear deformation theory of laminated elastic shells, International Journal of Engineering Science 1985, **23**, pp 319–330. https://doi.org/10.1016/0020-7225(85)90051-5.
29. SHEN, H.S. Postbuckling of nanotube-reinforced composite cylindrical shells in thermal environments, Part II: pressure-loaded shells, *Composites Structures*, 2011, **93**, pp 2096–2108. https://doi.org/10.1016/j.compstruct.2011.02.011.
30. SHEN, H.S. Postbuckling of nanotube-reinforced composite cylindrical shells in thermal environments, Part II: pressure-loaded shells, *Composites Structures*, 2011, **93**, pp 2496–2503. https://doi.org/10.1016/j.compstruct.2011.04.005.

31. NAVARRO, P., MARGUET, S., FERRERO, J.-F., BARRAU, J.-J. and LEMAIRE, S. Modeling of impacts on sandwich structures, *Mechanics of Advanced Materials and Structures*, 2012, **19**, pp 523–529. https://doi.org/10.1080/15376494.2011.556841.
32. ABRATE, S. Localized impact on sandwich structures with laminated facings, *Applied Mechanics Review*, 1997, **50**, pp 69. https://doi.org/10.1115/1.3101689.
33. KARAS, K. Platten unter seitlichem Stoss, *Ingenieur-Archive*, 1939, **10**, pp 237–50.
34. WU, H.-Y.T. and FU-KUO, C. Transient dynamic analysis of laminated composite plates subjected to transverse impact, *Computer & Structures*, 1989, **31**, pp 453–466. https://doi.org/10.1016-/0045-7949(89)90393-3.
35. KHALILI, S.M.R., MALEKZADEH, K. and GORGABAD, A.V. Low velocity transverse impact response of functionally graded plates with temperature dependent properties, *Composites Structures*, 2013, **96**, pp 64–74. https://doi.org/10.1016/j.compstruct.2012.07.035.
36. WU, H.-Y.T. Impact induced stresses, strains, and delaminations in composite plates, *J of Composite Materials*, 1988, **22**, pp 533–60.
37. SHEN, H.-S. and ZHANG, C.-L. Thermal buckling and postbuckling behavior of functionally graded carbon nanotube-reinforced composite plates, *Material Design*, 2010, **31**, pp 3403–3411. https://doi.org/10.1016/j.matdes.2010.01.048.
38. RICHARD, A.T., SMALLEY, E., COLBERT, D.T., GUO, T., RINZLER, A.G. and NIKOLAEV, P. Method of making ropes of single-wall carbon nanotubes, 2001.
39. BARRON, R.F. and BARRON, B.R. *Design for Thermal Stresses*, John Wiley & Sons, Hoboken, US, 2012.
40. SONG, Y.S. and YOUN, J.R. Modeling of effective elastic properties for polymer based carbon nanotube composites, *Polymer (Guildford)*, 2006, **47**, pp 1741–1748. https://doi.org/10.1016/j.polymer.2006.01.013.
41. BAYAT, M.R., RAHMANI, O. and MASHHADI, M.M. Nonlinear low-velocity impact analysis of functionally graded nanotube-reinforced composite cylindrical shells in thermal environments, *Polymers Composites*, 2018, 730–45, pp 1–16. https://doi.org/10.1002/pc.
42. REDDY, J.N. and CHIN, C.D. Thermomechanical analysis of functionally graded cylinders and plates, *J Thermal Stresses*, 1998, **21**, pp 37–41.
43. SHEN, H.-S. and XIANG, Y. Nonlinear vibration of nanotube-reinforced composite cylindrical shells in thermal environments, *Computer Methods in Applied Mechanics and Engineering*, 2012, **213–216**, pp 196–205. https://doi.org/10.1016/j.cma.2011.11.025.